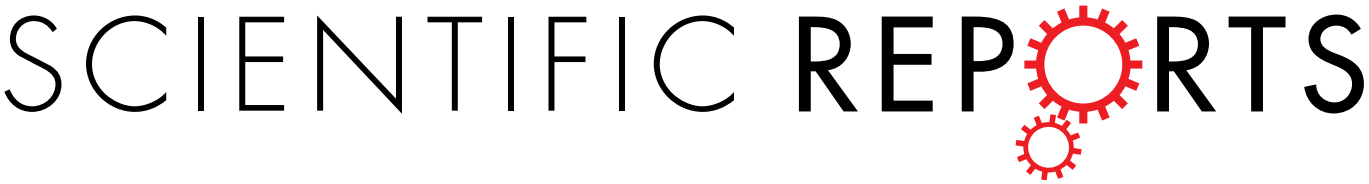

OPEN

Received: 9 January 2017
Accepted: 5 April 2017
Published online: 10 May 2017

Flexible and Self-Healing Aqueous Supercapacitors for Low Temperature Applications: Polyampholyte Gel Electrolytes with Biochar Electrodes

Xinda Li[1], Li Liu[1], Xianzong Wang[1], Yong Sik Ok[2], Janet A. W. Elliott[1], Scott X. Chang[3] & Hyun-Joong Chung[1]

A flexible and self-healing supercapacitor with high energy density in low temperature operation was fabricated using a combination of biochar-based composite electrodes and a polyampholyte hydrogel electrolyte. Polyampholytes, a novel class of tough hydrogel, provide self-healing ability and mechanical flexibility, as well as low temperature operation for the aqueous electrolyte. Biochar is a carbon material produced from the low-temperature pyrolysis of biological wastes; the incorporation of reduced graphene oxide conferred mechanical integrity and electrical conductivity and hence the electrodes are called biochar-reduced-graphene-oxide (BC-RGO) electrodes. The fabricated supercapacitor showed high energy density of 30 Wh/kg with ~90% capacitance retention after 5000 charge–discharge cycles at room temperature at a power density of 50 W/kg. At −30 °C, the supercapacitor exhibited an energy density of 10.5 Wh/kg at a power density of 500 W/kg. The mechanism of the low-temperature performance excellence is likely to be associated with the concept of non-freezable water near the hydrophilic polymer chains, which can motivate future researches on the phase behaviour of water near polyampholyte chains. We conclude that the combination of the BC-RGO electrode and the polyampholyte hydrogel electrolyte is promising for supercapacitors for flexible electronics and for low temperature environments.

Enhancing the low temperature performance of electrochemical storage devices is crucial in applications in automobiles, wearable devices, and energy grids in cold climates. At low temperatures (<−10 °C) such devices suffer various issues, including reduced ion transport due to increased viscosity and embrittlement of polymeric binder components[1]. For electrochemical capacitors, *i.e.*, supercapacitors, low temperature operation is established down to −40 °C, typically by using organic solvents or ionic liquids with low freezing points[2–4]. However, these liquids have other limitations, such as humidity dependent conductivity change, toxicity and environmental contamination when leaked, as well as high flammability and high vapor pressure, which may lead to hazardous explosions if local overheating occurs[5–9]. To mitigate potential hazards, active research is ongoing on aqueous electrolytes for energy storage devices, such as lithium ion[10] or sodium ion batteries[11], as well as supercapacitors[12] in order to develop safe energy storage devices, but low temperature operation for aqueous electrolytes has not been established. There is a critical need to develop electrochemical energy storage devices that have desirable performance characteristics at low temperatures, with both suitable electrolyte and electrode.

Gel polymer electrolytes, swollen polymers containing electrolyte solutions with proper solvents or plasticizers, possess superior properties such as self-supporting shape and fast ionic transport, properties possessed by solid and liquid electrolytes, respectively. Compared to liquid electrolytes, gel polymer electrolytes are intrinsically

[1]Department of Chemical and Materials Engineering, University of Alberta, Edmonton, Alberta, T6G 1H9, Canada. [2]School of Natural Resources and Environmental Science & Korea Biochar Research Center, Kangwon National University, Chuncheon, 24341, Korea. [3]Department of Renewable Resources, University of Alberta, Edmonton, Alberta, T6G 2H1, Canada. Correspondence and requests for materials should be addressed to H.-J.C. (email: chung.hj13@ualberta.ca)

free of leakage problems or the need for separators, reducing the requirement for costly special packaging[13]. Poly(vinyl alcohol) (PVA) is one of the widely used polymeric frameworks for aqueous gel polymer electrolytes with proton[14,15] or alkaline doping[16,17]. Potassium hydroxide (KOH) doped PVA hydrogels exhibit high ionic conductivities. However, the low temperature application of aqueous gel electrolytes is limited due to monolithic ice formation. Hydrogels from polyampholytes—polyelectrolytes containing both anion and cation groups in a single chain—possess desirable structural properties found in gel polymer electrolytes such as rubber-like elasticity, extreme tear resistance against crack propagation, self-healing ability and self-adjusting adhesion[18–20]. In addition, our parallel research showed that polyampholyte hydrogel electrolyte maintains mechanical flexibility at very low temperature by slush-like ice formation[21]; thus we envision making robust, flexible, and eco-friendly aqueous energy storage devices suitable for cold climates.

Carbon-based materials have been of intense interest as electrodes for making energy storage devices. While activated carbon from coconut shell is the current gold standard in the supercapacitor industry[22], carbon nanotubes and graphene have been extensively studied[23,24]. While most research focuses on nanostructure optimization for maximizing capacitance density by efficient ion transport and sieving, the key issue for industrial application lies in the optimal balance between material production cost and performance. In addition, low volumetric energy density caused by 'fluffiness' impedes the use of alternative carbon sources for making energy storage devices[22].

Biochar (BC) produced from agriculture waste by slow pyrolysis at low temperature (400~700 °C) has attracted attention for soil fertility improvement, carbon sequestration and water purification[25,26]. Recent studies show possibilities of using biochar in energy storage devices[27–29]. Pure BC is not suitable as an electrode material for three reasons: low specific capacitance, the powdery nature of the material, and low electrical conductivity. Nitric acid treatment and thermal flashing can increase the specific capacitance of exfoliated biochar electrodes from 2.1 to 221.3 $F g^{-1}$ [28]. Structural integrity and electrical conductivity are remedied by adding polymeric binders and conductive additives, respectively. These additional components make up a considerable fraction of the weight of electrodes, resulting in lower energy density and higher device cost[30–32].

In this paper, we report the fabrication of a flexible and self-healing aqueous supercapacitor for low temperature applications using polyampholyte and biochar as base materials for gel electrolyte and electrode, respectively. Specifically, we employed a polyampholyte hydrogel as an electrolyte for electrochemical energy storage for the first time due to its preferable mechanical properties such as stretchability, tear-resistance, adjustable adhesion, and self-healing ability. More importantly, we found that polyampholyte hydrogels (PA) prohibited monolithic ice formation; this leads to device flexibility in ice-forming temperatures, which will enable low temperature application of aqueous electrolytes as a cost-effective and eco-friendly solution for use in cold climates. For electrodes, we employed a soybean stover-based biochar with 7.5% (wt) reduced graphene oxide (BC-RGO) as a novel high-performance and cost-effective material. Using KOH to provide electrolytic ions, the polyampholyte-based supercapacitor (SC-PA) achieved specific capacitance of 193 $F g^{-1}$ at 0.5 $A g^{-1}$ with an energy density of 30 $Wh kg^{-1}$ at room temperature. At −30 °C, its energy density was 10.5 $Wh kg^{-1}$, which is remarkably higher than that of a control sample (3.4 $Wh kg^{-1}$) consisting of BC-RGO electrodes with an unconfined KOH solution in a cellulose separator as the electrolyte.

Results and Discussion

Device Fabrication: an Overview. Figure 1 summarizes the procedure for SC-PA fabrication. Pristine biochar processed from soybean stover (BC-pristine) is ground, sieved and acid treated (Fig. 1a). The treated biochar (BC-treated), however, is still in a powder form and is not electrically conductive. The addition of reduced graphene oxide (RGO) (7.5 wt%) provided a binder to maintain mechanical integrity and a conducting conduit for electrical conductivity. The composite is bendable and stretchable without powder disintegration, which is a suitable trait for making flexible devices. After bonding the composite electrode to a Kapton substrate (Fig. 1b), copolymerization of sodium 4-vinylbenzenesulfonate (NaSS) and [3-(methacryloylamino)propyl]trimethyl-ammoniumchloride (MPTC) on the BC-RGO film in a UV chamber synthesizes the hydrogel of poly(NaSS-co-MPTC), denoted as PA (Fig. 1c). Subsequently, the BC-RGO/PA pair is dialyzed in a 3 M KOH solution for 1 day (Fig. 1d). A symmetric supercapacitor is assembled by pressing together two BC-RGO electrodes without the use of a separator (Fig. 1e). Figure 1f describes the encapsulation process, which concludes the fabrication of the supercapacitor (SC-PA). A photograph of a SC-PA in operation is shown in Fig. 1g.

Electrode: Morphological Characterization. The morphological evolution of BC was examined by scanning electron microscopy (SEM) and transmission electron microscopy (TEM). The SEM images in Fig. 2a–d show that the milling and the acid treatment reduced the average powder size of BC from ~100 μm to ~10 μm. The TEM images show that the treatment generated an abundance of ~10 nm sized mesopores in BC-treated (Figure S2c), which is not found in BC-pristine (Figure S2a), with micropores and nanopores that are present all over the BC-treated (Figures S2d). The hierarchical porous structure is a clear indication of increased specific surface area. The top-view of the BC-RGO film (Fig. 2e and f) highlights that the BC particles were well wrapped by RGO, resulting in structural integrity. The continuous RGO networks also provide electrical conductivity for the electrode. The cross-sectional views of BC-RGO (Fig. 2g and h) indicate that the thickness of the electrode is ~40 μm. The BC-RGO contains macropores that can serve as ionic pathways for effective diffusion of electrolytes[31,33].

The Braunauer–Emmett–Teller (BET) nitrogen adsorption method was used to determine the surface area of BC materials. The adsorption isotherms (volume of nitrogen per gram of BC material at standard temperature and pressure (STP); Fig. 3a) reveal that the specific surface areas of BC-pristine and BC-treated were 187 and 414 $m^2 g^{-1}$, respectively, which is consistent with TEM results (Figure S2) and earlier studies on acid treated BC[28,

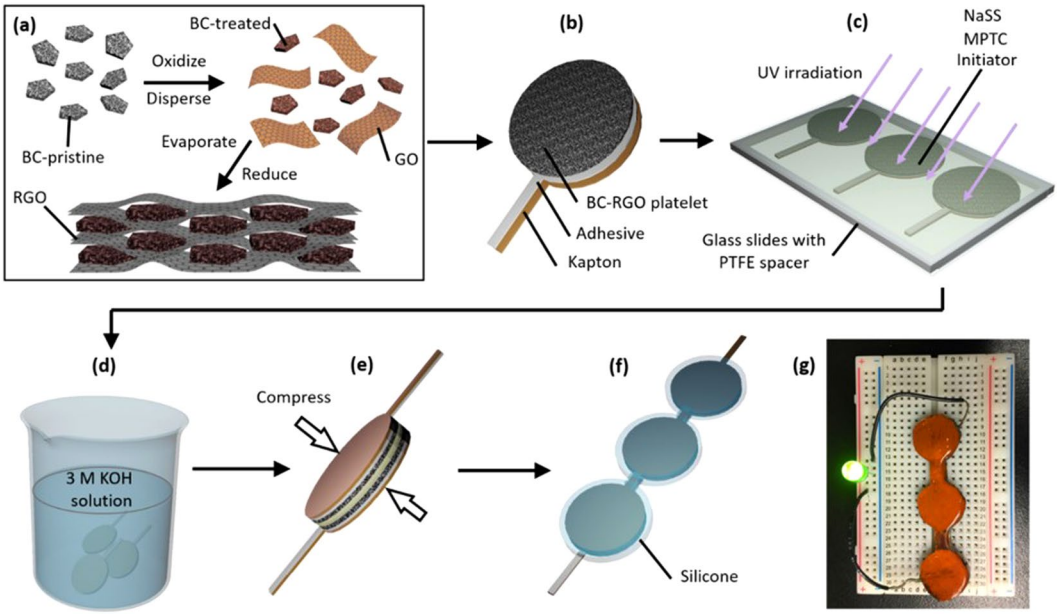

Figure 1. Schematic of supercapacitor (SC-PA) fabrication. (**a**) As-received biochar (BC-pristine) was oxidized (BC-treated) and dispersed in a graphene oxide solution. Subsequent solvent evaporation and graphene oxide reduction result in a consolidated electrode (BC-RGO) with high electrical conductivity. (**b**) The BC-RGO electrodes are supported on a Kapton substrate. (**c**) A polyampholyte hydrogel is synthesized on the BC-RGO electrodes by photo-initiated random copolymerization of NaSS and MPTC. (**d**) The electrolyte is dialyzed in 3 M KOH solution. (**e**) Compressing the dialyzed electrolyte/electrode pair with the top BC-RGO electrode will make a symmetric supercapacitor. (**f**) Three symmetric supercapacitors are encapsulated in silicone to light a green LED in (**g**).

[34]. The RGO wrapping further increased the specific surface area to 483 $m^2 g^{-1}$. The pore size distribution of the microspores and mesopores were evaluated by Non-Local Density Functional Theory (NLDFT) (an indicator of pore size distribution; Fig. 3b). For all three samples, there exists a sharp peak at 1.5 nm and a broad peak ranging from 2 to 4 nm, and the peak heights increase from BC-pristine to BC-treated, then to BC-RGO. It is notable that nanometer-scale mesopores (TEM image; Figure S2c) and macropores (Fig. 2h) are also abundant in BC-RGO, indicating a hierarchical porous structure suitable for SC electrodes[35].

Electrochemical Test of BC-RGO Electrodes. The electrochemical properties of BC-RGO electrodes were evaluated using three electrodes with Ag/AgCl as a reference electrode. The results of cyclic voltammetry (CV) profiles at different scan rates, galvanostatic charging/discharging (GCD) at different current densities, electrochemical impedance spectroscopy (EIS), and CV performance in various aqueous electrolytes are shown in Figure S4. In all cases, no obvious redox peaks were observed. The general characteristics of CV plots were similar to prior studies on pyrolyzed biomass in KOH (Figure S4a)[36–38]. The symmetric triangle shape of the GCD profiles implies reversibility and stability of electrode materials (Figure S4b). At a current density of 0.5 A g^{-1}, the specific capacitance of BC-RGO electrodes reached 216 F g^{-1} (183 F cm^{-3}). The capacitance retention was 76% at 6 A g^{-1}. The specific surface area normalized capacitance was 44.62 μF cm^{-2} at 0.5 A g^{-1}. From the Nyquist plot, the equivalent series resistance (ESR) in the high-frequency region was ~0.6 Ω (Figure S4c)[39]. Detailed discussions can be found in the Supplementary Information.

Performance of SC-PA at Room Temperature. In order to evaluate the efficacy of the polyampholyte hydrogel as a gel electrolyte material, we devised a control sample that employs a liquid aqueous KOH solution with a cellulose separator as an electrolyte (SC-KOH; configuration shown in Figure S5). The polymer, water, and KOH concentrations of control samples were tuned to be same as the polyampholyte-KOH electrolyte, by precisely controlling the amount of KOH solution in the cellulose separator. Figure 4a shows the CV profiles of SC-PA with scan rates ranging from 5 to 100 mV s^{-1}. The curves display a quasi-rectangular and symmetric shape. Figure 4b presents the GCD curves of SC-PA at current densities ranging from 0.5 to 6 A g^{-1}. At 0.5 and 6 A g^{-1}, the specific capacitances of BC-RGO were 193 and 141 F g^{-1}, respectively. At a current density of 2 A g^{-1}, a capacitance retention of ~90% was obtained after 5000 successive GCD cycles (Fig. 4c).

Energy density and power density are important properties of a supercapacitor. The Ragone plots of SC-PA and SC-KOH are compared with previous studies on biomass-based symmetric supercapacitors with aqueous electrolytes (Figure S7). The SC-PA has energy densities of 30.3, 23.4, and 11.9 Wh kg^{-1} at power densities of 50 W kg^{-1}, 1 kW kg^{-1}, and 12 kW kg^{-1}, respectively. The energy density of SC-PA is comparable to other published supercapacitors that employ coconut shell-based electrodes (state-of-the-art)[40], as well as other biomass-based electrodes[37,41]. It should be noted that the activated carbon materials mentioned were produced at 800 °C followed

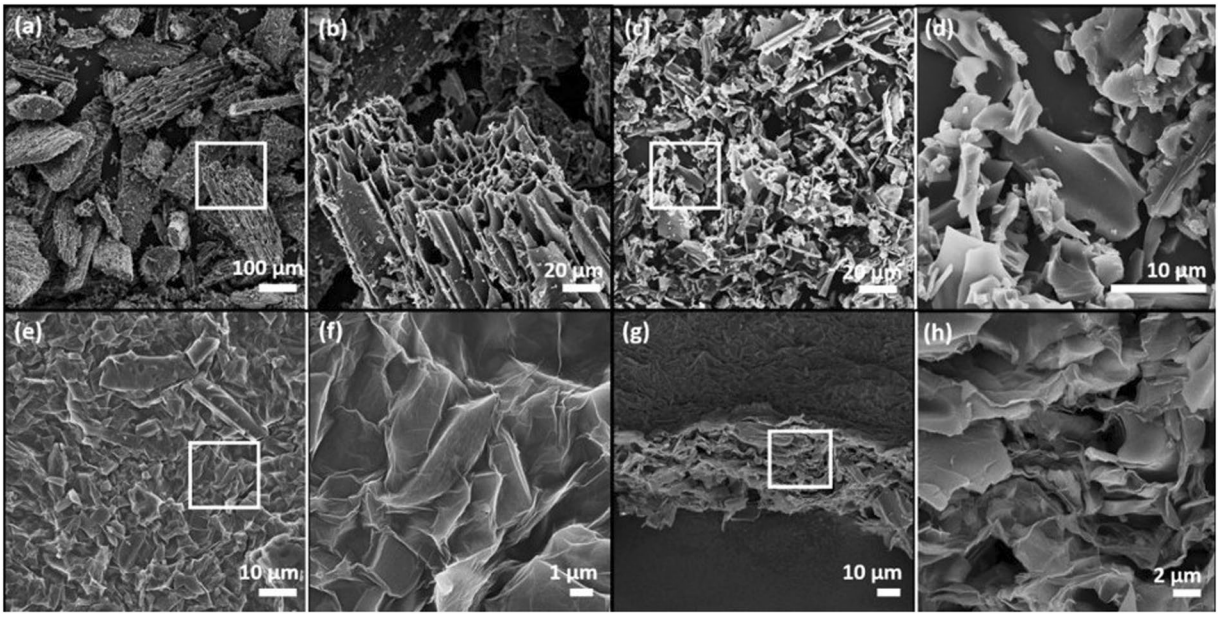

Figure 2. (**a**) The SEM image of as-received biochar (BC-pristine) and (**b**) a magnified image of the small region identified by the white rectangular box in (**a**). (**c**) The SEM image of oxidized biochar (BC-treated) and (**d**) a magnified image of the small region identified in (**c**). (**e**) The SEM image of the top of a BC-RGO electrode and (**f**) a magnified image of the small region identified in (**e**). (**g**) The SEM image of the BC-RGO cross section and (**h**) a magnified image of the small region identified in (**g**).

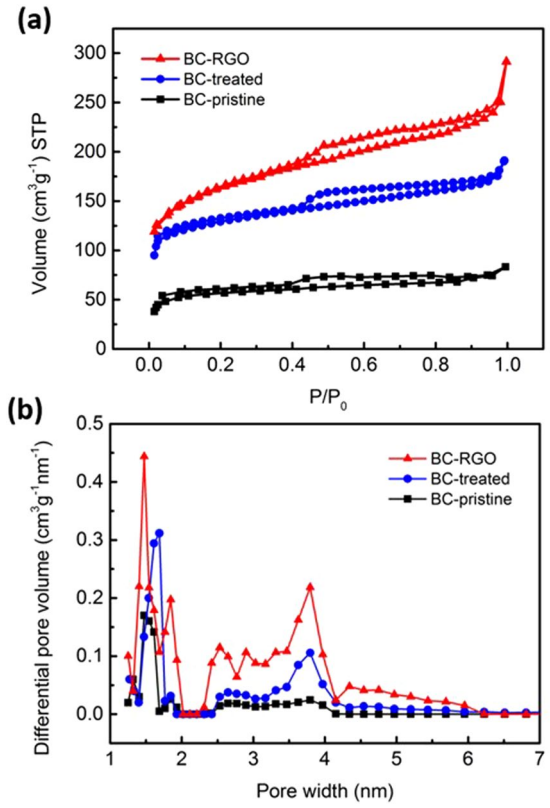

Figure 3. (**a**) Nitrogen adsorption isotherm according to the BET model and (**b**) Pore size distribution (represented as differential pore volume plotted against pore width) derived from (**a**), calculated with the NLDFT model.

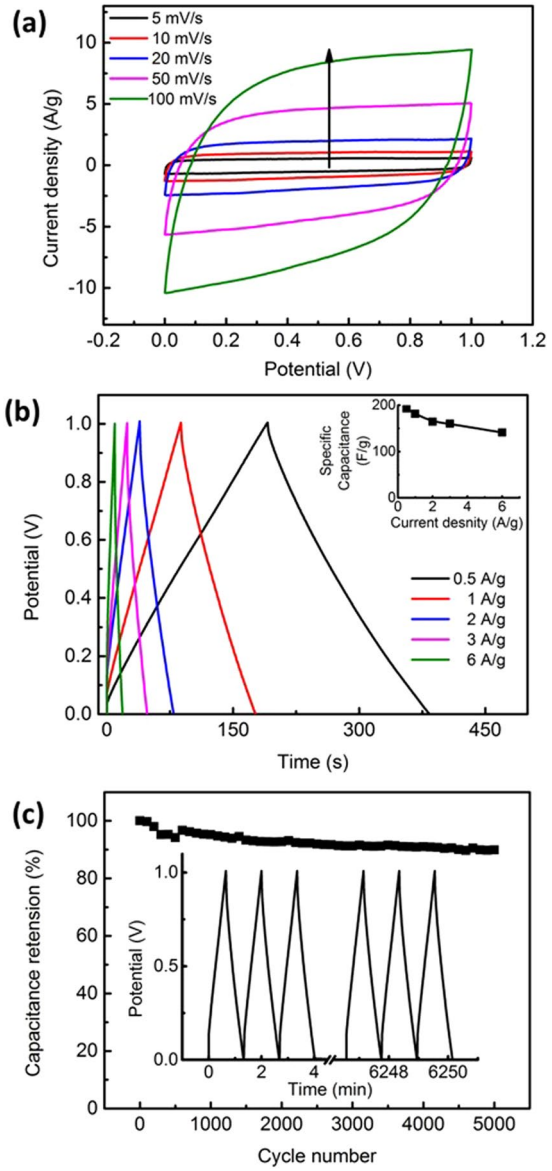

Figure 4. (**a**) Cyclic voltammetry (CV) and (**b**) galvanostatic charging–discharging (GCD) profiles of symmetric SC-PA KOH (inset: specific capacitance verses current density). The arrow in (**a**) indicates the direction of increasing scanning rate. (**c**) Cycle test of the fabricated supercapacitor (SC-PA). The inset presents first and last three galvanostatic charging–discharging (GCD) profiles.

by chemical activation, and the values calculated were on the basis of active components in electrodes; typically, 5–20% of the total electrode mass is binders or conductive additives, which do not exist in our device.

Performance of the Supercapacitor at Low Temperature. The performance of the SC-PA was evaluated at temperatures ranging from 20 to −30 °C. Figure 5a shows the CV profiles of the SC-PA at different temperatures. The sweep rate was fixed at 20 mV s^{-1}. With a decreasing temperature, the area enveloped by the CV curve decreased, while the increased resistance to ionic transport caused the shape of the cycle to deviate from a quasi-rectangle. Figure 5b shows the GCD curves of the SC-PA at a charging–discharging current of 1 A g^{-1}. Calculated specific capacitance verses temperature is given as an inset in the same figure. The values were 175, 163, 149, 132, 102, and 75 F g^{-1} at temperatures of 20, 10, 0, −10, −20, and −30 °C, respectively. The energy density of the SC-PA was 10.5 Wh kg^{-1} at a power density of 500 W kg^{-1}. As indicated by the CV curves shown in the Supplementary Information (Figure S8), the specific capacitance of the control SC-KOH was only 24 F g^{-1} at −30 °C, where the energy density was 3.4 Wh kg^{-1} at a power density of 500 W kg^{-1}, which is only 32% of the performance of the SC-PA at the same temperature. It is notable that the only difference between the SC-PA and the SC-KOH is the media that contains the aqueous solution of KOH; the polyampholyte network contains KOH in the SC-PA in a hydrogel form, whereas the separator that is used for the SC-KOH leaves the aqueous solution as a liquid. As mentioned in the previous discussion, the room temperature performance is shown to be comparable

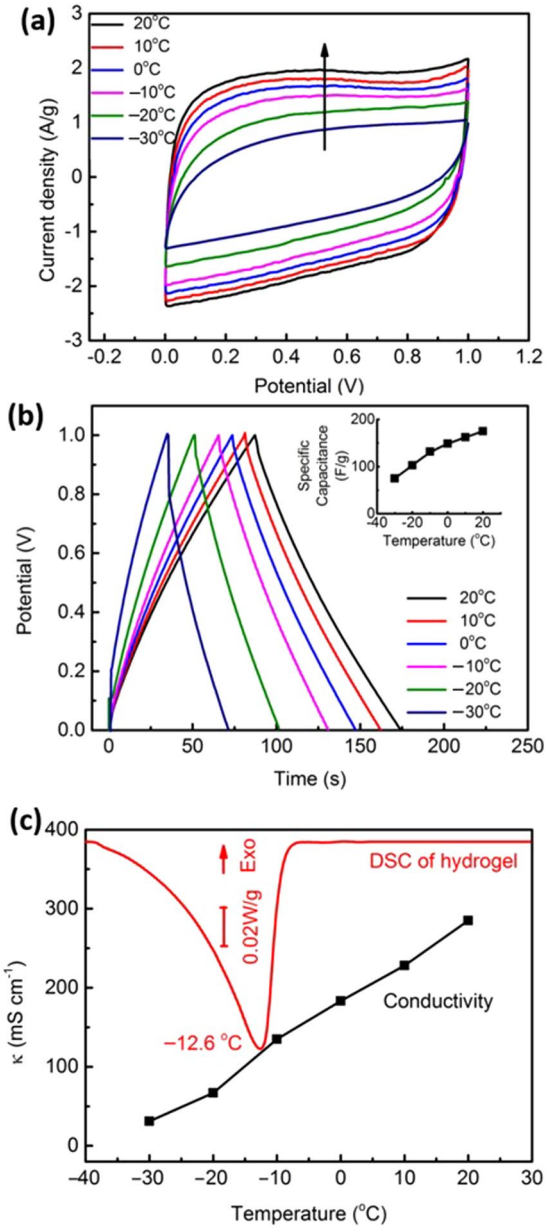

Figure 5. (**a**) Fabricated supercapacitor (SC-PA) temperature dependence of cyclic voltammetry (CV) profiles at a scan rate of 20 mV s^{-1}. The arrow indicates the direction of increasing temperatures. (**b**) Galvanostatic charging–discharging (GCD) profiles at a current density of 1 A g^{-1}. The inset indicates calculated specific capacitance with respect to temperature change. (**c**) A differential scanning calorimetry (DSC) result of 3 M KOH-containing polyampholyte hydrogel with increasing temperature compared with the change in conductivity as a function of temperature.

to the state-of-the-art values. And the electrochemical performance of the polyampholyte supercapacitor at low temperature was close to the values of other non-aqueous electrolyte supercapacitors reported at temperatures around −30 °C, without worries about electrolyte leakage[2–4]. The specific capacitance of the activated graphene based supercapacitors in ionic liquid electrolyte was ~100 F g^{-1} at a scanning rate of 1 mV s^{-1} [2]. And specific capacitances of an ionogel-based solid-state supercapacitor were 68 and 34 F g^{-1} operating at −20 and −40 °C, respectively, at a scanning rate of 5 mV s^{-1} [42]. To our knowledge, a specific capacitance comparable to that of our polyampholyte supercapacitor at subzero temperature has never been reported before in the literature for other aqueous-based electrolyte supercapacitor, or conventional solid-state supercapacitor using PVA-KOH gel or other gels[24]. Plus, due to the unique structure of polyampholyte networks in the hydrogel[21], the device is still flexible at subzero temperature, which will be discussed later in this paper.

In order to understand the underlying mechanism of the improvement in supercapacitor performance at −30 °C, we performed a differential scanning calorimetry (DSC) measurement for a polyampholyte that contained the same concentration of KOH as in the SC-PA (Fig. 5c). It is well known that water molecules

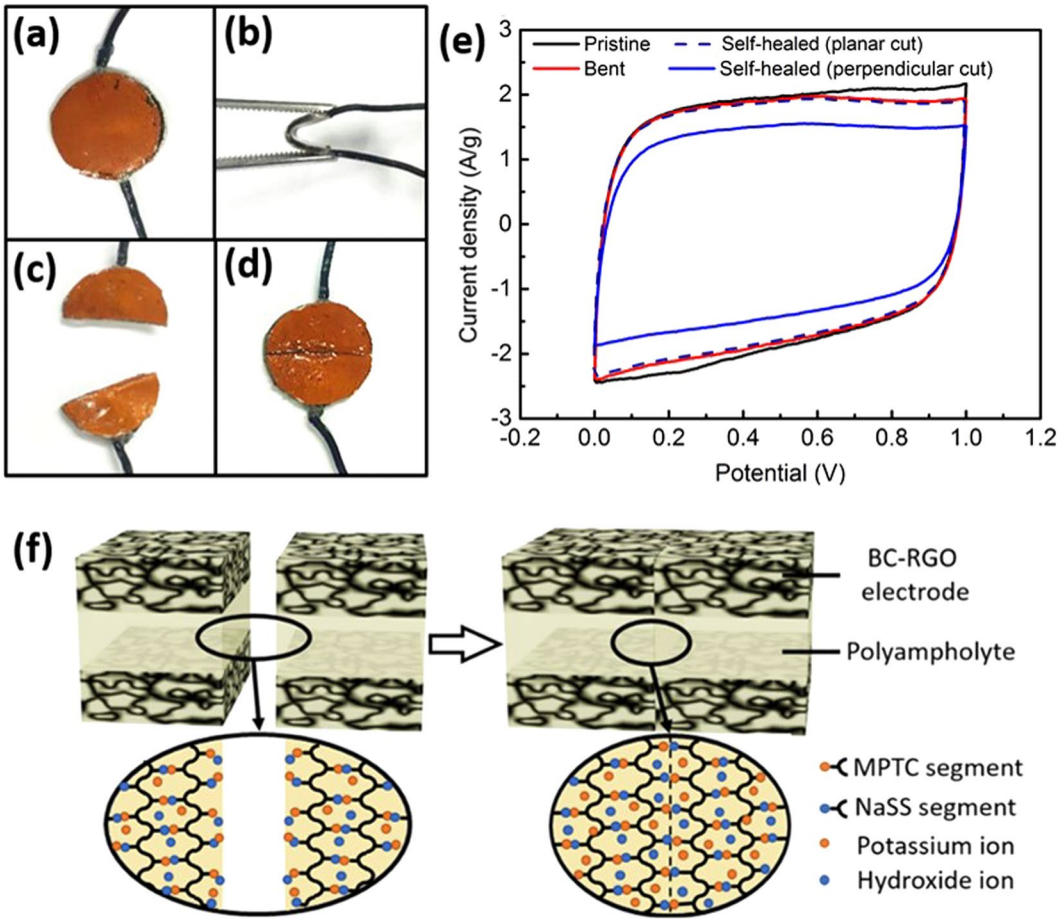

Figure 6. Photographs of (**a**) pristine, (**b**) bent, (**c**) broken, and (**d**) self-healed supercapacitor (SC-PA). (**c**,**d**) show the procedure for the perpendicular cut. The procedure for the planar cut is described in supporting information. (**e**) Cyclic voltammetry (CV) profile of pristine, bent and self-healed (perpendicular and planar cuts) SC-PAs at a scan rate of 20 mV s^{-1}. (**f**) Schematic illustration of polyampholyte hydrogel self-healing for the perpendicular cut.

strongly adsorbed on hydrophilic polymer chains cannot participate in ice formation, and thus are classified as 'non-freezable water' that can be found unfrozen down to −190 °C[43,44]. Likewise, strongly bound water on ionic species will form hydrated ions and will not freeze as ice, but the hydrated KOH will freeze at its eutectic temperature of −60.9 °C[45]. Based on these assumptions, we froze all 'freezable water' at −60.0 °C for 10 minutes, followed by bringing up the temperature to +10 °C at a slow rate of +1 °C per minute. An endothermal peak started to appear at −39.5 °C, reached a peak at −12.6 °C, and ended at −6.2 °C. The fraction of water molecules that participated in the freezing–thawing cycle was quantified by the area under the peak; here, 23.6% of water molecules were frozen at −60.0 °C. A control experiment with an aqueous solution of KOH held in place with a separator reveals that 30.4% of water molecules were frozen at the same temperature. It is unclear at the moment whether the 6.8% of the water molecules that could not be frozen due to polyampholyte chains accounted for the supercapacitor performance enhancement. The measured ionic conductivity in Fig. 5c reveals that the conductivity is a strong function of temperature, but the formation of ice is not the only dominant factor determining the change in ionic conduction. One hypothesis for the improved supercapacitor performance, however, is that the morphology of ice is connected to the performance and that the crosslinked network structure of the polyampholyte chains disrupts the crystalline growth of ice. The 'slush ice model' is consistent with the fact that KOH containing polyampholyte hydrogel is still flexible whereas an aqueous KOH solution is a rigid monolithic ice at −30 °C. In our parallel study[21], we showed that the hierarchical nanostructure of polyampholyte hydrogel allows both polymer-rich (yet highly hydrated) and polymer-poor (yet populated with polymer strands) domains. Vogt *et al.* measured fast dynamics of local diffusivity of water molecules in hydrogel networks at extremely low temperatures (220 K), which shed light to the mechanism of our enhanced supercapacitor performance at low temperatures[46]. Future investigations that identify structure–property relations of polyampholyte hydrogels at low temperatures may shed light on the mechanism.

Mechanical Flexibility and Self-Healing Properties. The pristine SC-PA (Fig. 6a) was bent to a radius of curvature of 5 mm (Fig. 6b), showing nearly no degradation in supercapacitor performance (Fig. 6e). The self-healing ability was tested by cutting the SC-PA into two pieces (perpendicular cut; Fig. 6c), followed by a

self-healing process (Figure S9a). The self-healed SC-PA (Fig. 6d) showed ~80% of capacitance compared to the control (non-cut) device (Fig. 6e). The 20% loss of capacitance of the self-healed SC-PA may be attributed to slight mismatch in overlapping of the broken BC-electrodes, resulting in an increase of ESR. As another example of self-healing, the SC-PA was sliced into two pieces by splitting the polyampholyte hydrogel electrolyte in the planar direction (planar cut; Figure S9b). After self-healing, the CV result almost exactly reproduced the control sample result, indicating a perfect self-healing (Fig. 6e). The self-healing ability can be attributed to the reversible nature of ionic crosslinking in polyampholyte hydrogels[18,19], as illustrated in Fig. 6f. The bendable and self-healing nature of the SC-PA is promising for wearable and flexible electronics applications of the supercapacitor.

Conclusions

A supercapacitor with a high energy density that works at low temperature was fabricated with a combination of BC-RGO electrodes and a polyampholyte hydrogel. Reduced graphene oxide was incorporated with biochar to transform the pyrolyzed waste biomass into high performance binder-free electrodes for electrochemical energy storage devices. The specific capacitance of BC-RGO was 216 F g^{-1} at a current density of 0.5 A g^{-1} in the three-electrode configuration. The electrochemical performance can be further improved using biochar with higher specific surface area or by doping transition metal oxide[47–49]. A symmetric supercapacitor made with BC-RGO as the electrode and polyampholyte hydrogel as the electrolyte showed a high energy density of 30 Wh kg^{-1}, and a capacitance retention of ~90% after 5000 charge–discharge cycles. At low temperature (−30 °C), the SC-PA had an energy density of 10.5 Wh kg^{-1} at a power density of 500 W kg^{-1}, which is a clear improvement over the performance of SC-KOH at the same temperature owing to the use of polyampholyte as a hydrogel hosting material of the aqueous KOH electrolyte, showing a potential for energy storage, even for grid-scale solutions at low temperature[50]. The flexibility and self-healing properties indicate the possible application of SC-PA in flexible and wearable devices.

Material and Methods

Biochar Preparation. Soybean stover was collected from agricultural fields in Korea as a model agricultural waste. The soybean stover was dried (at 60 °C), sieved (2 mm), and then pyrolyzed at 700 °C with a heating rate of 7 °C min^{-1} under anoxic conditions.

Fabrication of BC-Treated. BC-pristine was ground and sieved to obtain fine powder (325 mesh). The powder was treated with nitric acid (35% in water) at 75 °C for 4 h, filtered, and rinsed with deionized water and ethanol[27,28]. Drying in a convection oven at 120 °C overnight concluded the fabrication of BC-treated.

Fabrication of BC-RGO Electrodes. BC-treated was added into a graphene oxide (GO) solution (4 mg GO mL^{-1}, Graphenea, Spain). Here, 50 mg BC-treated was added to each milliliter of the GO solution. The mixture was cast on a glass plate at 80 °C for quick evaporation of the solvent. The dried BC-GO film was cut into platelet shapes 15 mm in diameter. As described in our previous paper[51], the BC-GO platelet was reduced by an aqueous solution of L-ascorbic acid (Vitamin-C, 8 mg mL^{-1}, Sigma-Aldrich, US). The reaction was done with a distillation apparatus in an oil bath at 95 °C. After 4 hours of reaction, the platelet was dialyzed in deionized water to remove remaining ascorbic acid. Then, the platelet was dried for an hour in a convection oven at 120 °C. The mass of each platelet was approximately 10 mg. The reduced platelet is denoted as BC-RGO. After that, the platelet was attached to a Kapton sheet (15 mm diameter, DuPont, US) to conclude the BC-RGO electrode fabrication.

Synthesis of Polyampholyte Hydrogel on a BC-RGO Electrode. For polyampholyte synthesis, we followed a protocol by Gong *et al.*[18], who developed a one-step random copolymerization of sodium 4-vinylbenzenesulfonate (cationic monomer; NaSS) and [3-(methacryloylamino)propyl] trimethylammonium chloride (anionic monomer; MPTC) with 2-hydroxy-4′-(2-hydroxyethoxy) -2-methylpropiophenone (photoinitiator). The chemicals were purchased from Sigma-Aldrich and used as received. The aqueous solution of 1 M NaSS, 1 M MPTC and 0.001 M photoinitiator was injected into the gap between two glass plates, where the gap was separated by a Teflon spacer (thickness 250 μm). Here, one of the glass plates had an attached BC-RGO electrode. A 2 hour irradiation with a UV lamp (broadband light with a maximum peak at 365 nm; Jelight, US) transforms the precursor solution into polyampholyte hydrogel. The hydrogel is denoted as PA. After the gelation, the BC-RGO/PA pair were peeled off of the glass plate, and then dialyzed in a 3 M potassium hydroxide (KOH) solution for 12 h.

Assembly of Symmetric Supercapacitor. The symmetric supercapacitor was assembled by bonding the two BC-RGO/PA constructs by compression. The self-healing property of the PA facilitated the bonding process. The symmetric supercapacitor was dipped into a commercial room-temperature vulcanizing silicone (Shin-Etsu, Japan) for packaging. The silicone was cured for an hour to conclude the fabrication of the symmetric supercapacitor (SC-PA). A control sample of symmetric supercapacitor (SC-KOH), where the electrolyte is a 3 M aqueous solution of KOH, was also fabricated. In the control sample, the two BC-RGO electrodes are separated by a cellulose paper with macroscopic (~25 μm) open pores.

Characterization of BC-RGO Electrodes. A field emission scanning electron microscope (FE-SEM; Zeiss Sigma) was utilized for the morphological study along with a high-resolution transmission electron microscope (HR-TEM; JEOL 2200FS). X-ray diffraction (XRD) patterns were recorded on a Rigaku RU-200B X-ray diffractometer with a rotating anode X-ray generator using Cu Kα radiation (40 kV, 110 mA). X-ray photoelectron spectroscopy (XPS) was carried out on a Kratos Axis spectrometer with monochromatized Al Kα. The C1s peak at 284.6 eV was used to calibrate all XPS spectra. A Renishaw In Via microscope system was used to collect Raman spectra from samples. A 785 nm diode laser was used as an excitation source. Surface area and porosity were

investigated using nitrogen adsorption at 77 K (Autosorb-iQ, Quantachrome Instruments, US). Specific surface area was calculated from the BET adsorption isotherm and pore size distribution was calculated by NLDFT based on a slit-pore model; the calculations were done with a built-in software (ASiQwin). The electrical conductivity was evaluated with a four-point probe station (Pro4-4400, Lucas Signatone Corporation, CA, US) connected to a Keithley 2400 source measure unit.

Electrochemical Measurements. The BC-RGO electrodes were tested in a three-electrode configuration in 3 M KOH electrolyte, where a platinum counter electrode and an Ag/AgCl reference electrode were used. Cyclic voltammetry (CV), galvanostatic charge–discharge (GCD) cycling and electrochemical impedance spectroscopy (EIS) were performed with an electrochemical station (1285 A/1260 A, Solartron, UK). The frequency range for EIS measurement was from 0.1 MHz to 10 mHz, where an open circuit potential mode with an AC perturbation of 5 mV was used. The durability of the BC-RGO electrodes was evaluated by applying 5000 successive GCD cycles at a current density of 2 A g^{-1}. The specific capacitance (C_s) of the BC-RGO electrode was calculated from the GCD curve using Equation 1:

$$C_s = \frac{I\Delta t}{m\Delta V} \tag{1}$$

where I is the GCD current, Δt is the discharge time, m is the mass of the BC-RGO electrode (excluding mass of the Kapton substrate), and ΔV is the potential window after the correction for IR–drop.

The symmetric supercapacitors were tested in a two-electrode configuration. The BC-RGO electrode capacitance was evaluated from the GCD curve using Equation 2:

$$C_s = \frac{2I\Delta t}{m\Delta V} \tag{2}$$

Here, the equivalent series resistance (ESR) of the supercapacitor was calculated by IR-drop in the galvanostatic charge–discharge curves as in Equation 3:

$$ESR = \frac{V_{\mathrm{IR-drop}}}{I} \tag{3}$$

Two key factors of a supercapacitor, the gravimetric energy density (E) and the power density (P), are evaluated from the discharge curves of the GCD at different current densities using Equations 4 and 5 [52]:

$$E = I\int \frac{\Delta V dt}{2m} \tag{4}$$

$$P = \frac{E}{\Delta t} \tag{5}$$

Conductivity values of the electrolyte at temperatures ranging from +20 °C to −30 °C were measured in the cell placed in a Peltier stage (TS102G, Instec Inc.), as described in the Supporting Information (Figure S1). Ionic conductivity is calculated according to Equation 6:

$$\kappa = \frac{c}{R_s} \tag{6}$$

where c is the cell constant, and R_s is the solution resistance at 60 KHz measured by EIS. To ensure that equilibrium was reached at a specific temperature, R_s values were collected after the output became stable. Likewise, supercapacitor performances (CV, GCD, and EIS) at a specific temperature were measured after 10 minutes of stabilization time.

Differential Scanning Calorimetry (DSC) Measurements. The relative amount of freezable and non-freezable water in neat 3 M KOH solution in water and in the solution in the polyampholyte hydrogel (*i.e.*, PA) were quantified by differential scanning calorimetry (DSC, Q1000, TA Instruments, US). The samples were tested immediately after preparation to prevent any possible loss of water through evaporation. For each measurement, 10 mg of sample was sealed in a copper sample pan. For each DSC measurement, the following thermal history was programmed: (i) temperature held at 10 °C for 10 min, (ii) cooled from +10 to −60 °C at a rate of 1 °C min^{-1}, (iii) held at −60 °C for 10 min, (iv) heated to 10 °C at a rate of 1 °C min^{-1}. Here, we utilized the data from the heating cycle. The frozen water content can be calculated using Equation 7 [53]:

$$F_{\mathrm{frozen},T} = \frac{\Delta H_{\mathrm{m},T}}{\Delta H_{\mathrm{m}}^{0}(1 - C)} \tag{7}$$

where $F_{\mathrm{frozen,T}}$ is the fraction of frozen water at temperature T, $\Delta H_{\mathrm{m}}^{0}$ is the melting enthalpy of pure water, $\Delta H_{\mathrm{m}}^{0} = 333.5$ J g^{-1}, and C is the polymer concentration in polyampholyte hydrogel, which is calculated by Equation 8:

$$C = \frac{m_{\text{dried}}}{m_{\text{pristine}}} \tag{8}$$

where m_{dried} is the mass of freeze-dried hydrogel, and m_{pristine} is the mass of as-prepared hydrogel that contained 3 M KOH solution.

References

1. Tarascon, J. M. & Armand, M. Issues and challenges facing rechargeable lithium batteries. *Nature* **414**, 359–367, doi:10.1038/35104644 (2001).
2. Tsai, W. Y. *et al*. Outstanding performance of activated graphene based supercapacitors in ionic liquid electrolyte from −50 to 80 °C. *Nano Energy* **2**, 403–411, doi:10.1016/j.nanoen.2012.11.006 (2013).
3. Lin, R. *et al*. Capacitive energy storage from −50 to 100 °C using an ionic liquid electrolyte. *J. Phys. Chem. Lett.* **2**, 2396–2401, doi:10.1021/jz201065t (2011).
4. Brandon, E. J., West, W. C., Smart, M. C., Whitcanack, L. D. & Plett, G. A. Extending the low temperature operational limit of double-layer capacitors. *J. Power Sources.* **170**, 225–232, doi:10.1016/j.jpowsour.2007.04.001 (2007).
5. Armand, M., Endres, F., MacFarlane, D. R., Ohno, H. & Scrosati, B. Ionic-liquid materials for the electrochemical challenges of the future. *Nat. Mater.* **8**, 621–629, doi:10.1038/nmat2448 (2009).
6. Ranke, J. *et al*. Lipophilicity parameters for ionic liquid cations and their correlation to *in vitro* cytotoxicity. *Ecotoxicol. Environ. Saf.* **67**, 430–438, doi:10.1016/j.ecoenv.2006.08.008 (2007).
7. Tang, S., Baker, G. A. & Zhao, H. Ether- and alcohol-functionalized task-specific ionic liquids: attractive properties and applications. *Chem. Soc. Rev.* **41**, 4030–4066, doi:10.1039/c2cs15362a (2012).
8. Zhao, D., Liao, Y. & Zhang, Z. Toxicity of ionic liquids. *Clean-Soil Air Water* **35**, 42–48, doi:10.1002/(ISSN)1863-0650 (2007).
9. Quartarone, E. & Mustarelli, P. Electrolytes for solid-state lithium rechargeable batteries: recent advances and perspectives. *Chem. Soc. Rev.* **40**, 2525–2540, doi:10.1039/c0cs00081g (2011).
10. Luo, J. Y., Cui, W. J., He, P. & Xia, Y. Y. Raising the cycling stability of aqueous lithium-ion batteries by eliminating oxygen in the electrolyte. *Nat. Chem.* **2**, 760–765, doi:10.1038/nchem.763 (2010).
11. Pan, H., Hu, Y. S. & Chen, L. Room-temperature stationary sodium-ion batteries for large-scale electric energy storage. *Energy Environ. Sci.* **6**, 2338–2360, doi:10.1039/c3ee40847g (2013).
12. Wang, F. *et al*. Electrode materials for aqueous asymmetric supercapacitors. *RSC Adv.* **3**, 13059–13084, doi:10.1039/c3ra23466e (2013).
13. Yang, P. & Mai, W. Flexible solid-state electrochemical supercapacitors. *Nano Energy.* **8**, 274–290, doi:10.1016/j.nanoen.2014.05.022 (2014).
14. Meng, C., Liu, C., Chen, L., Hu, C. & Fan, S. Highly flexible and all-solid-state paperlike polymer supercapacitors. *Nano Lett.* **10**, 4025–4031, doi:10.1021/nl1019672 (2010).
15. Yu, H. *et al*. A novel redox-mediated gel polymer electrolyte for high-performance supercapacitor. *J. Power Sources* **198**, 402–407, doi:10.1016/j.jpowsour.2011.09.110 (2012).
16. Yang, C. C., Hsu, S. T. & Chien, W. C. All solid-state electric double-layer capacitors based on alkaline polyvinyl alcohol polymer electrolytes. *J. Power Sources* **152**, 303–310, doi:10.1016/j.jpowsour.2005.03.004 (2005).
17. Yang, C. C. & Lin, S. Preparation of alkaline PVA-based polymer electrolytes for Ni–MH and Zn–air batteries. *J. Appl. Electrochem.* **33**, 777–784, doi:10.1023/A:1025514620869 (2003).
18. Sun, T. L. *et al*. Physical hydrogels composed of polyampholytes demonstrate high toughness and viscoelasticity. *Nat. Mater.* **12**, 932–937, doi:10.1038/nmat3713 (2013).
19. Ihsan, A. B. *et al*. Self-healing behaviors of tough polyampholyte hydrogels. *Macromolecules* **49**, 4245–4252, doi:10.1021/acs.macromol.6b00437 (2016).
20. Roy, C. K. *et al*. Self-adjustable adhesion of polyampholyte hydrogels. *Adv. Mater.* **27**, 7344–7348, doi:10.1002/adma.201504059 (2015).
21. Li, X., Banik, S., Elliott, J. A. W., Lee, B. and Chung, H.-J. Polymer structure and water states in salt-containing tough polyampholyte hydrogels, submitted (2017).
22. Weinstein, L. & Dash, R. Supercapacitor carbons. *Mater. Today* **16**, 356–357, doi:10.1016/j.mattod.2013.09.005 (2013).
23. Béguin, F., Presser, V., Balducci, A. & Frackowiak, E. Carbons and electrolytes for advanced supercapacitors. *Adv. Mater.* **26**, 2219–2251, doi:10.1002/adma.v26.14 (2014).
24. Lu, X., Yu, M., Wang, G., Tong, Y. & Li, Y. Flexible solid-state supercapacitors: design, fabrication and applications. *Energy Environ. Sci.* **7**, 2160–2181, doi:10.1039/c4ee00960f (2014).
25. Lehmann, J. A handful of carbon. *Nature* **447**, 143–144, doi:10.1038/447143a (2007).
26. Ok, Y. S., Chang, S. X., Gao, B. & Chung, H. J. SMART biochar technology—A shifting paradigm towards advanced materials and healthcare research. *Environ. Technol. Innovation* **4**, 206–209, doi:10.1016/j.eti.2015.08.003 (2015).
27. Jiang, J. *et al*. Highly ordered macroporous woody biochar with ultra-high carbon content as supercapacitor electrodes. *Electrochim. Acta.* **113**, 481–489, doi:10.1016/j.electacta.2013.09.121 (2013).
28. Genovese, M., Jiang, J., Lian, K. & Holm, N. High capacitive performance of exfoliated biochar nanosheets from biomass waste corn cob. *J. Mater. Chem. A* **3**, 2903–2913, doi:10.1039/C4TA06110A (2015).
29. Wang, H. *et al*. Interconnected carbon nanosheets derived from hemp for ultrafast supercapacitors with high energy. *ACS Nano* **7**, 5131–5141, doi:10.1021/nn400731g (2013).
30. Sumboja, A., Foo, C. Y., Wang, X. & Lee, P. S. Flexible and free-standing reduced graphene oxide/manganese dioxide paper for asymmetric supercapacitor device. *Adv. Mater.* **25**, 2809–2815, doi:10.1002/adma.201205064 (2013).
31. Xiong, Z., Liao, C., Han, W. & Wang, X. Mechanically tough large-area hierarchical porous graphene films for high-performance flexible supercapacitor applications. *Adv. Mater.* **27**, 4469–4475, doi:10.1002/adma.v27.30 (2015).
32. Xu, Y. *et al*. A metal-free supercapacitor electrode material with a record high volumetric capacitance over 800 F cm^{-3}. *Adv. Mater.* **27**, 8082–8087, doi:10.1002/adma.201504151 (2015).
33. Maiti, U. N., Lim, J., Lee, K. E., Lee, W. J. & Kim, S. O. Three-dimensional shape engineered, interfacial gelation of reduced graphene oxide for high rate, large capacity supercapacitors. *Adv. Mater.* **26**, 615–619, doi:10.1002/adma.v26.4 (2014).
34. Yin, C. Y., Aroua, M. K. & Daud, W. M. A. W. Review of modifications of activated carbon for enhancing contaminant uptakes from aqueous solutions. *Sep. Purif. Technol.* **52**, 403–415, doi:10.1016/j.seppur.2006.06.009 (2007).
35. Xia, K., Gao, Q., Jiang, J. & Hu, J. Hierarchical porous carbons with controlled micropores and mesopores for supercapacitor electrode materials. *Carbon* **46**, 1718–1726, doi:10.1016/j.carbon.2008.07.018 (2008).
36. Fan, L. Z., Chen, T. T., Song, W. L., Li, X. & Zhang, S. High nitrogen-containing cotton derived 3D porous carbon frameworks for high-performance supercapacitors. *Sci. Rep.* **5**, 15388, doi:10.1038/srep15388 (2015).
37. Xu, J. *et al*. Preparing two-dimensional microporous carbon from Pistachio nutshell with high areal capacitance as supercapacitor materials. *Sci. Rep.* **4**, 5545, doi:10.1038/srep05545 (2014).

38. Liu, B. *et al*. Nitrogen-doped banana peel-derived porous carbon foam as binder-free electrode for supercapacitors. *Nanomaterials* **6**, 18, doi:10.3390/nano6010018 (2016).
39. Stoller, M. D. & Ruoff, R. S. Best practice methods for determining an electrode material's performance for ultracapacitors. *Energy Environ. Sci.* **3**, 1294–1301, doi:10.1039/c0ee00074d (2010).
40. Mi, J., Wang, X. R., Fan, R. J., Qu, W. H. & Li, W. C. Coconut-shell-based porous carbons with a tunable micro/mesopore ratio for high-performance supercapacitors. *Energy & Fuels* **26**, 5321–5329 (2012).
41. Zhao, Y. Q. *et al*. Hierarchically porous and heteroatom doped carbon derived from tobacco rods for supercapacitors. *J. Power Sources* **307**, 391–400, doi:10.1016/j.jpowsour.2016.01.020 (2016).
42. Negre, L., Daffos, B., Turq, V., Taberna, P. L. & Simon, P. Ionogel-based solid-state supercapacitor operating over a wide range of temperature. *Electrochim. Acta.* **206**, 490–495, doi:10.1016/j.electacta.2016.02.013 (2016).
43. Takeshita, Y., Becker, E., Sakata, S., Miwa, T. & Sawada, T. States of water absorbed in water-borne urethane/epoxy coatings. *Polymer* **55**, 2505–2513, doi:10.1016/j.polymer.2014.03.027 (2014).
44. Ping, Z., Nguyen, Q., Chen, S., Zhou, J. & Ding, Y. States of water in different hydrophilic polymers–DSC and FTIR studies. *Polymer* **42**, 8461–8467, doi:10.1016/S0032-3861(01)00358-5 (2001).
45. Khodakovsky, I. L., Mironenko, M. V., Chernysheva, I. V. and Pokrovsky, O. S. Liquid radioactive waste solutions. In *Contaminant hydrology: cold regions modelling* (eds Grant, S. A. & Iskandar, I. K.) (CRC Press, 2000).
46. Wiener, C. G., Tyagi, M., Liu, Y., Weiss, R. A. & Vogt, B. D. Supramolecular hydrophobic aggregates in hydrogels partially inhibit ice formation. *J. Phys. Chem. B* **120**, 5543–5552, doi:10.1021/acs.jpcb.6b02863 (2016).
47. Jian, Z. *et al*. A high-power symmetric Na-ion pseudocapacitor. *Adv. Funct. Mater.* **25**, 5778–5785, doi:10.1002/adfm.201502433 (2015).
48. Zhu, Y. *et al*. Porous $NiCo_2O_4$ spheres tuned through carbon quantum dots utilised as advanced materials for an asymmetric supercapacitor. *J. Mater. Chem. A* **3**, 866–877, doi:10.1039/C4TA05507A (2015).
49. Zhu, Y. *et al*. A carbon quantum dot decorated RuO2 network: outstanding supercapacitances under ultrafast charge and discharge. *Energy Environ. Sci.* **6**, 3665–3675, doi:10.1039/c3ee41776j (2013).
50. Pasta, M., Wessells, C. D., Huggins, R. A. & Cui, Y. A high-rate and long cycle life aqueous electrolyte battery for grid-scale energy storage. *Nat. Commun.* **3**, 1149, doi:10.1038/ncomms2139 (2012).
51. Li, X. *et al*. Sponge-templated macroporous graphene network for piezoelectric ZnO nanogenerator. *ACS Appl. Mater. & Interf.* **7**, 20753–20760, doi:10.1021/acsami.5b05702 (2015).
52. Arbizzani, C., Mastragostino, M. & Soavi, F. New trends in electrochemical supercapacitors. *J. Power Sources* **100**, 164–170, doi:10.1016/S0378-7753(01)00892-8 (2001).
53. Li, W., Zheng, Y. & Cheng, R. Transition of hydration states of poly (vinyl alcohol) in aqueous solution. *Polymer* **49**, 4740–4744, doi:10.1016/j.polymer.2008.08.029 (2008).

Acknowledgements

The authors gratefully acknowledge funding from NSERC (RGPIN 435914, CHRPJ 478519) and CIHR (CPG 140186) through Discovery and Collaborative Health Research Project programs. J.A.W.E. holds a Canada Research Chair in Thermodynamics. Material characterization was partly done in the shared facility of the NanoFAB in the Faculty of Engineering at the University of Alberta. We thank Prof. Jingli Luo for discussions and equipment support and Ms. Kangyi Lou for help with biochar processing.

Author Contributions

X.L. and H.-J.C. conceived ideas. Y.-S.O. and S.X.C. fabricated and provided the pristine biochar. J.A.W.E. contributed in developing the hydrogel electrolyte. X.L. fabricated the biochar electrode, the hydrogel electrolyte, and the supercapacitor device. X.L., L.L. and X.W. characterized the materials and the device. X.L. and H.-J.C. drafted the manuscript. J.A.W.E., Y.-S.O. and S.X.C. provided critical revisions of the manuscript. All coauthors approved the final version of the manuscript for publication.

Additional Information

Supplementary information accompanies this paper at doi:10.1038/s41598-017-01873-3

Competing Interests: The authors declare that they have no competing interests.

Publisher's note: Springer Nature remains neutral with regard to jurisdictional claims in published maps and institutional affiliations.

Supporting Information

Flexible and Self-Healing Aqueous Supercapacitors for Low Temperature Applications: Polyampholyte Gel Electrolytes with Biochar Electrodes

Xinda Li[a], Li Liu[a], Xianzong Wang[a], Yong Sik Ok[b], Janet A.W. Elliott[a], Scott X. Chang[c], Hyun-Joong Chung[,a]*

[a] Department of Chemical and Materials Engineering, University of Alberta, Edmonton, Alberta, T6G 1H9, Canada
[b] School of Natural Resources and Environmental Science & Korea Biochar Research Center, Kangwon National University, Chuncheon, 24341, Korea
[c] Department of Renewable Resources, University of Alberta, Edmonton, Alberta, T6G 2H1, Canada

* Corresponding Author:
E-mail: chung.hj13@ualberta.ca (H.-J. Chung), phone: +1-780-492-4790

S1) Experimental setup for low temperature measurements

Figure S1 shows photographs of the experimental setup. The written description can be found in the Experimental Section of the main text.

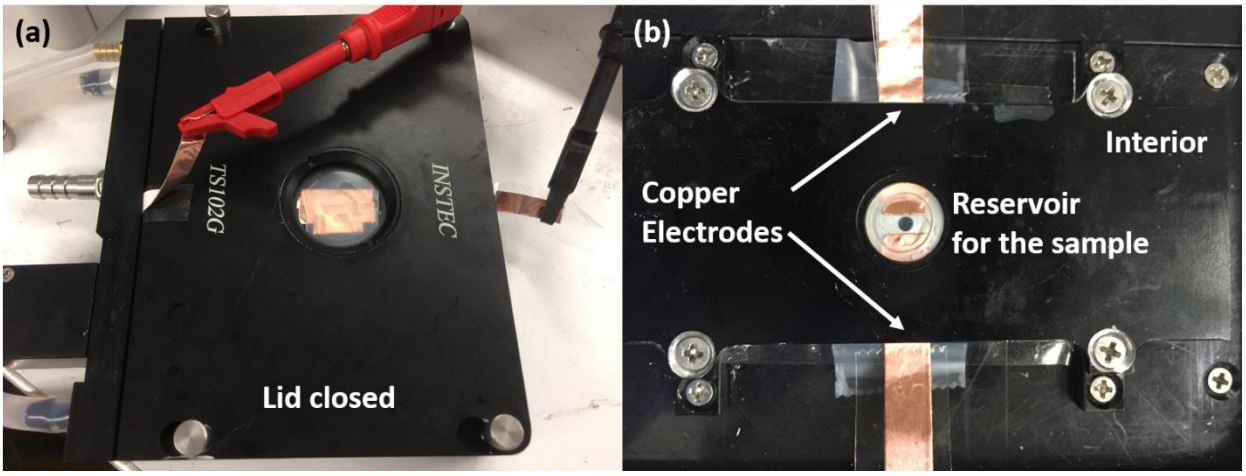

Figure S1. (a) Exterior and (b) interior pictures of our experimental setup for ionic conductivity measurement in the range between –30 to +20 °C.

S2) TEM images of BC-pristine, BC-treated and BC-RGO

For transmission electron microscope (TEM) sample preparation, 10 mg of BC-pristine (biochar at an as-received status; **Figures S2a** and **S2b**) or BC-treated (biochar after the treatment described in the Experimental Section; **Figures S2c** and **S2d**) was added to 20 mL ethanol and sonicated for 10 min. For the BC-RGO electrode (7.5 wt% RGO), the whole electrode was ground into powder before being dispersed in the ethanol. A droplet of the mixture was applied on TEM copper mesh, while any excess amount was removed with Kimwipes. The copper mesh was dried overnight in a convection oven at 120 °C.

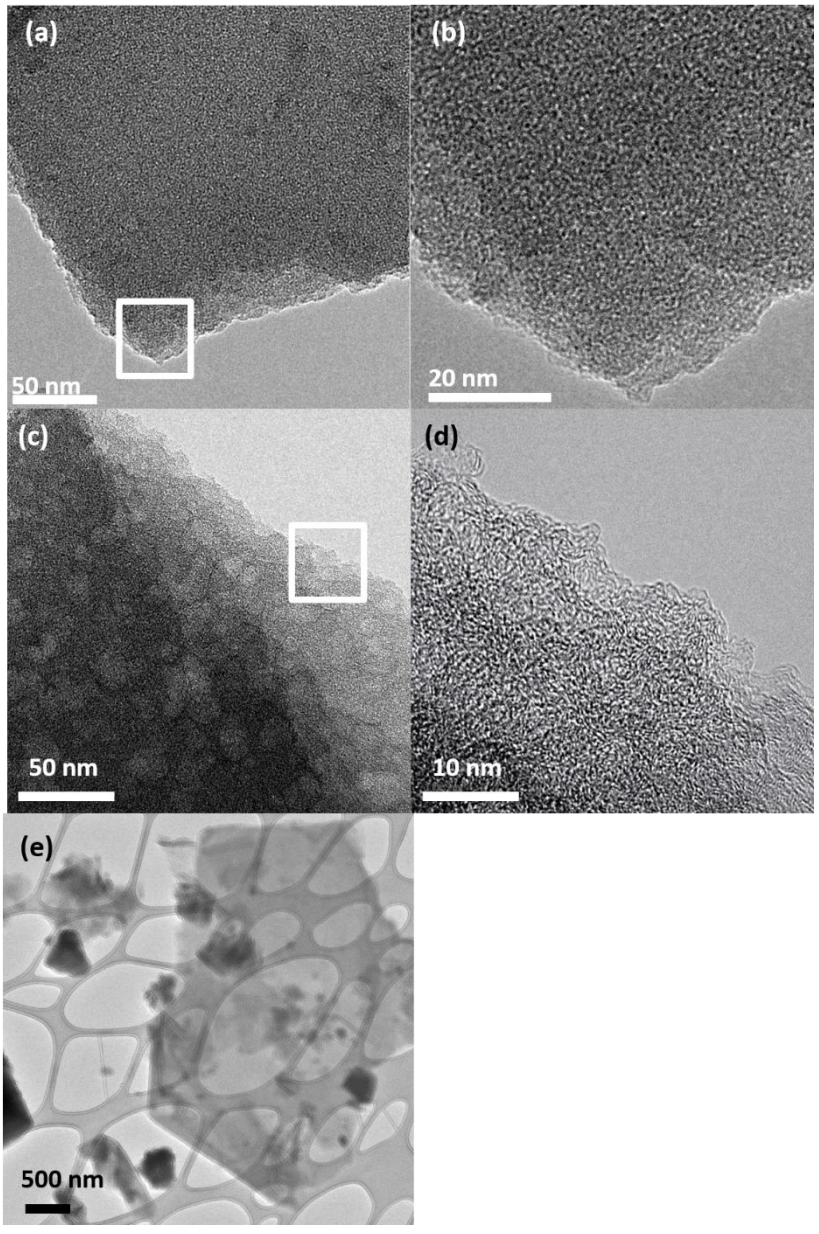

Figure S2. High resolution TEM images of BC-pristine ((a) and (b)), BC-treated ((c) and (d)), and low-resolution TEM image of BC-RGO (e). The white rectangles in the low magnification images, (a) and (c), indicate the regions of imaging in (b) and (d), respectively. See main text for discussion.

S3) Chemical analysis and electrical conductivity of biochar: Effects of treatment

Details of the measurement conditions (equipment and operation modes) can be found in the Experimental Section of the main text.

The chemical compositions at the surfaces of samples were investigated by X-Ray Photoelectron Spectroscopy (XPS). As summarized in **Table S1**, the carbon content of BC-pristine was 75.9%, with 2.4% nitrogen and 21.7% oxygen atoms. After nitric acid treatment, the oxygen and nitrogen contents were both increased to 24.0% and 4.6%, respectively. High resolution spectra of N1s (**Figure S3a**) indicates the existence of three main surface nitrogen species, pyridinic nitrogen (~398.5 eV), pyridonic nitrogen (~ 400.2 eV) and nitrate (~407.3 eV) [1, 2]. The BC-treated samples exhibited dramatically increased nitrate signal compared to the BC-pristine, possibly indicating adsorbed nitric acid after the treatment. After the reduction process by L-ascorbic acid, the peak at ~406 eV disappeared, but a strong peak of surface nitrogen oxide group was detected in the BC-RGO (the material for supercapacitor electrode; a composite of BC-treated and reduced graphene oxide). The effect of the acid treatment was further studied by analyzing C1s spectra (**Figure S3b**). The fitting suggests that the BC-treated samples have significant existence of C=O (~288.5 eV) and the amount of C-O bonding was noticeably increased as evidenced by the peak at 285.6 eV [3]. The existence of C-O bonding after the reduction by L-ascorbic acid (~285.8 eV) suggests that there are remaining hydroxyl groups on the surface of BC-RGO; we observed such a trend in our previous work [4]. It is notable that the hydroxyl groups on the surface can increase the apparent capacitance of the electrode by introducing the pseudo-capacitive effect of the quinone/hydroquinone redox pair [5, 6].

Raman spectroscopy was used to probe the bonding structure of the carbonaceous materials. There are four distinguishable bands presented in **Figure S3c**. First, the D-mode (disordered band) is located between 1330 and 1360 cm^{-1}. Second, the G-mode (tangential mode), which corresponds to the stretching mode in the graphite plane, is located at 1580 cm^{-1}. As the third and fourth bands, the second-order modes, 2D and D+G, are located at 2680–2690 and 2910–3220 cm^{-1}, respectively [8, 9]. The relative intensity of D-mode and G-mode (I_D/I_G) depends strongly on the density of defects in the graphitic material. A larger I_D/I_G suggests a higher density of sp^3 carbon due to structural defects [9]. The values of I_D/I_G decreased from 1.66 to 1.57 after the acid treatment, indicating that the structure of carbon in BC-treated is more ordered compared to that of BC-pristine, probably due to the reduction of impurities that causes the formation of amorphous carbon [10]. The intensities of 2D and D+G are also increasing from BC-pristine, to BC-treated, then to BC-RGO, indicating that the structure became more ordered as the fabrication process proceeded.

XRD patterns of BC-pristine, BC-treated, and BC-RGO are displayed in **Figure S3d**. All three samples showed two broad humps at around $2\theta = 24°$ and 43°, which are attributed to the (002) and (110) planes of graphitic carbon [11]. It is notable that BC-pristine exhibits a strong peak at $2\theta = 31°$, which belongs to a carbon allotrope with a six-fold helical chain structure whereas the bonding is entirely sp^2 hybridization [12]. Such a 6-fold peak was not observed in BC-treated and in BC-RGO, indicating a purification effect of the acid treatment.

A four-point probe measurement was used to evaluate the electrical conductivities of BC-pristine, BC-treated and BC-RGO. Here, 0.1 g of the powder of each BC was compressed into platelets at a pressure of 10 MPa. The thickness values of the platelets were obtained by cross-sectional SEM. The measured electrical conductivity values are shown in the last column of **Table S1**. The electrical conductivities of BC-pristine and BC-treated were 1.5 ± 0.2 $S \cdot m^{-1}$ and 0.20 ±

0.03 S·m^{-1}, respectively. After the introduction of the RGO, the conductivity value is dramatically increased to 531 ± 27 S m^{-1}. The moderately high conductivity of the powder material is very similar to the previously reported value for a KOH activated RGO electrode, which resulted in similar electrochemical performance as an electrode material for supercapacitors [17]. The scanning rate could be further increased by decreasing the electrode mass during CV [18]. This indicates that the RGO network provides an excellent conduit for electrons, and thus can serve as a charge collector in the electrochemical electrode.

Table S1. Summary of physical and chemical properties of various biochar (BC) samples.

Samples	S_{BET} [a] [m^{2}g^{-1}]	V_{NLDFT} [a] [cm^{3}g^{-1}]	C% [b]	N% [b]	O% [b]	I_D/I_G [c]	σ [d] [S m^{-1}]
BC-pristine	187	0.076	75.9	2.4	21.7	1.7	1.5 ± 0.2
BC-treated	414	0.26	71.4	4.6	24.0	1.6	0.20 ± 0.03
BC-RGO	483	0.35	81.5	0.8	17.7	2.0	531 ± 27

[a] Specific surface area and pore size as deduced from the adsorption isotherms in **Figure 3a**.
[b] Atomic percentage of C, O, and N as obtained from the sizes of XPS peaks.
[c] Intensity ratio between D and G bands as calculated from the Raman spectra in **Figure S3c**.
[d] Electrical conductivity values as obtained from four-point probe measurements.

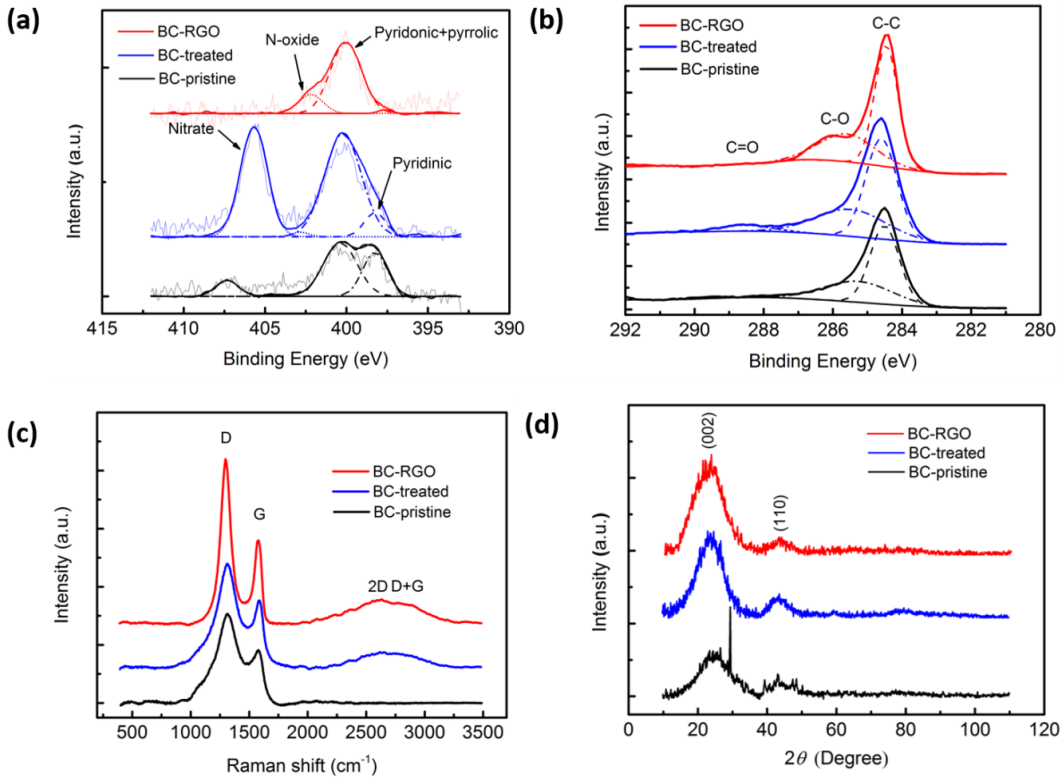

Figure S3. Chemical analysis of various biochar (BC) samples. X-ray photoelectron spectroscopy (XPS) profiles near (a) N1s and (b) C1s peaks. (c) Raman spectroscopy profiles. (d) X-ray diffraction (XRD) profiles.

S4) Electrochemical properties of BC-RGO electrodes as evaluated by the three-electrode configuration

In order to evaluate the efficacy of BC-RGO as an electrode material for supercapacitors, the three-electrode configuration measurement was performed in a 3 M KOH aqueous solution as a model electrolyte. Here, the BC-RGO was the working electrode, whereas Ag/AgCl and Pt electrodes were serving as the reference and the counter electrodes, respectively. The cyclic voltammetry (CV) results are shown in **Figure S4a.** The potential window for each voltage cycle was from –0.9 V to +0.1 V (with respect to Ag/AgCl). Various scanning rates between 5 and 100 mV s^{-1} were evaluated. No obvious redox peaks were observed in the selected potential window. **Figure S4b** gives the GCD profile of BC-RGO electrodes at varying current. The linearity in the output and charging and discharging cycle (the symmetric triangle shape of the output) implies the reversibility and stability of electrode materials during operation. The specific capacitance versus current density values are shown as the inset in **Figure S4b**; specific capacitance values were calculated from the discharging time. At current density of 0.5 A g^{-1}, the specific capacitance of the BC-RGO reached 216 F g^{-1}. The specific capacitance decreased as the current increased. One explanation is that the drop in specific capacitance of BC-RGO electrode at high current density was due to the transport behavior of ions in electrolyte when confined in the hierarchical nanostructure of electrodes. At low current density, the ions can find enough time to diffuse through the hierarchical porous structure of the BC-RGO electrodes. At high current density, the ionic transport into the nanostructures of the electrode may cause delay in redox interactions (i.e. the charge transport to the electrolyte–electrode interface becomes the rate-determining process). The rather sudden drop of specific capacitance at high current density is an issue for future study; the performance can be further enhanced by finding the right feedstock for the biochar and/or by optimizing the processing conditions for electrode fabrication. The capacitance value normalized by specific surface area was 44.62 μF cm^{-2} at 0.5 A g^{-1}. The high surface capacitance was possibly contributed to by the abundant surface functional groups, which can cause pseudo-capacitance effects. The hierarchical porous structure of BC-RGO, where macroscopic pores provide a high diffusion path for electrolytes and meso- and nanoscopic pores provide high specific surface area, is also beneficial to make the majority of pores accessible for electrochemical reactions. Moreover, the absence of binder and conductive additives enables the complete use of surface area on the surface of BC-RGO to store electrochemical energy. The Nyquist plot from an electrochemical impedance spectroscopy (EIS) measurement of BC-RGO (**Figure S4c**) comprised a semicircle in the high-frequency region and a linear plot in the low-frequency region. The equivalent series resistance (ESR) obtained by extrapolating the curve from the high-frequency region of the Nyquist plot to intersect the real-axis was only ~ 0.6 Ω. The approximately vertical line in the low-frequency region indicates fast ion transfer in aqueous electrolytes. The CV measurements of BC-RGO in various aqueous electrolyte systems were also performed (**Figure S4d**). The CV profiles show that the BC-RGO electrodes have the highest specific capacitance in 3 M KOH solution.

The results for BC-RGO electrodes with different loading amounts of RGO in the electrode were added as Figure S4e. Here, we observed that the BC-RGO provided larger specific capacitance when the electrode contained more BC-treated. The pure RGO electrodes show lower capacitance than those of BC-containing electrodes, and this can be attributed to self-aggregation or re-stacking of RGO sheets, as pointed out in previous literature [19]. Another point to consider is the mechanical integrity of the resulting BC-RGO electrode. The electrodes with RGO equal to or less than this critical value were fragile and they were occasionally broken into pieces during

the reduction in the ascorbic acid solution. Thus, even though BC-RGO electrodes with 5 wt% of RGO showed better electrochemical performance than those with 7.5 wt% RGO, the devices were fabricated with BC-RGO electrodes with 7.5 wt% RGO in the following parts of this paper.

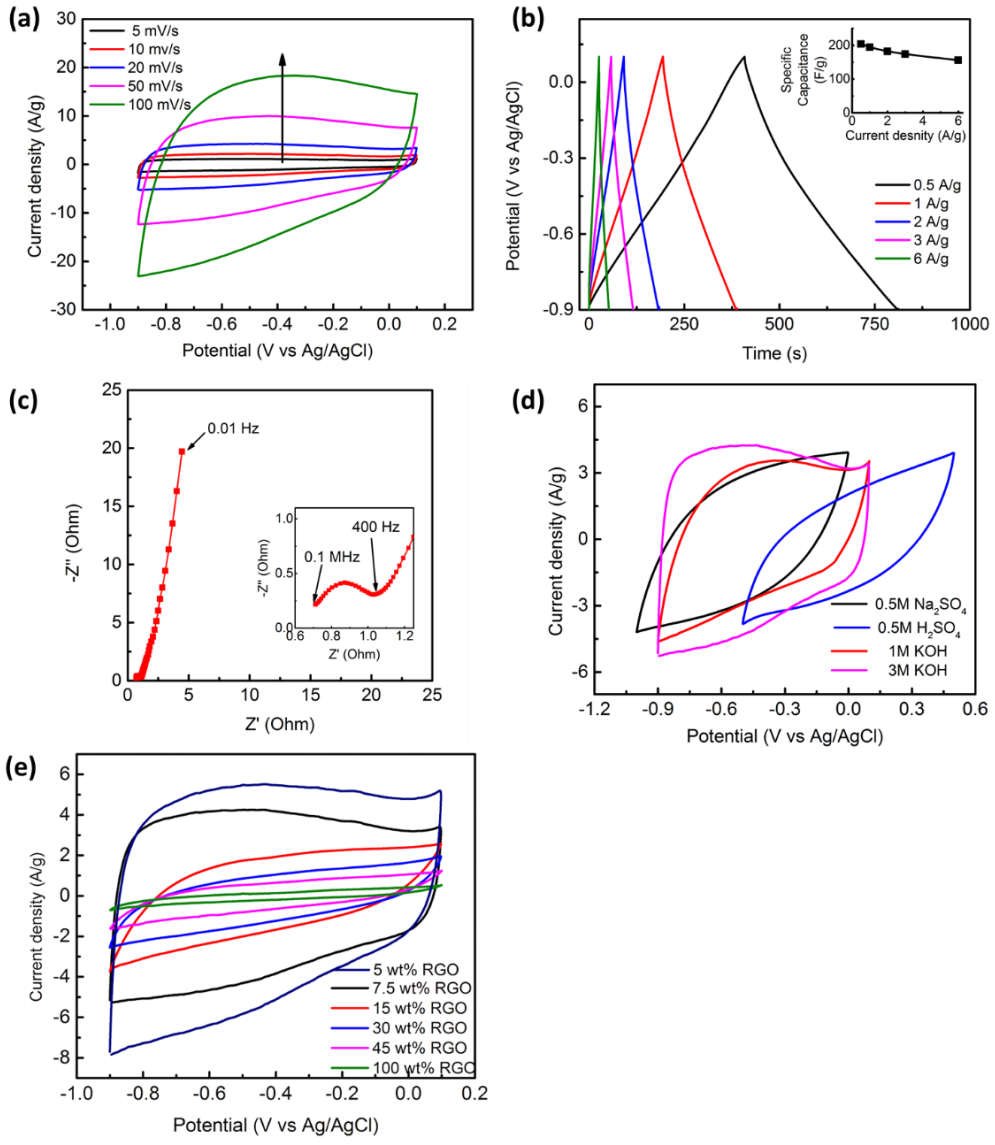

Figure S4. (a) Cyclic voltammetry (CV) profiles (b) Galvanostatic charging–discharging (GCD) profiles (inset: specific capacitance verses current density) and (c) the Nyquist plot of EIS measured in 3 M KOH aqueous electrolyte system. (d) CV of BC-RGO in different aqueous electrolytes at a scan rate of 20 mV s^{-1}. (e) CV of BC-RGO with different RGO weight percent in 3 M KOH solution at a scan rate of 20 mV s^{-1}.

S5) Device configuration of symmetric supercapacitor built with an unconfined 3 M KOH solution (SC-KOH) as the electrolyte

This sample was devised as a control sample to evaluate the efficacy of polyampholyte hydrogel as an aqueous gel electrolyte material for supercapacitors (SC-PA). Details about the fabrication and characteristics of the SC-PA control symmetric supercapacitor can be found in the main text and the following sections in the Supporting Information.

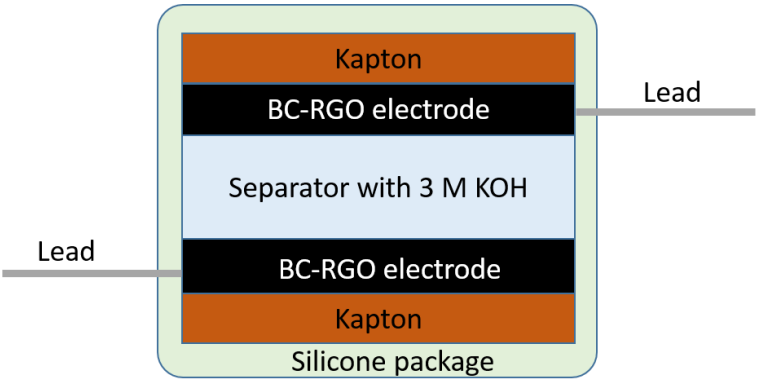

Figure S5. Device configuration of SC-KOH.

S6) Electrochemical characterizations of SC-KOH

Figures S6a and **S6b** show CV and GCD curves of SC-KOH, respectively. **Figure S6c** also compares the Nyquist plots of SC-PA and SC-KOH. ESR of SC-KOH was 0.86 Ω.

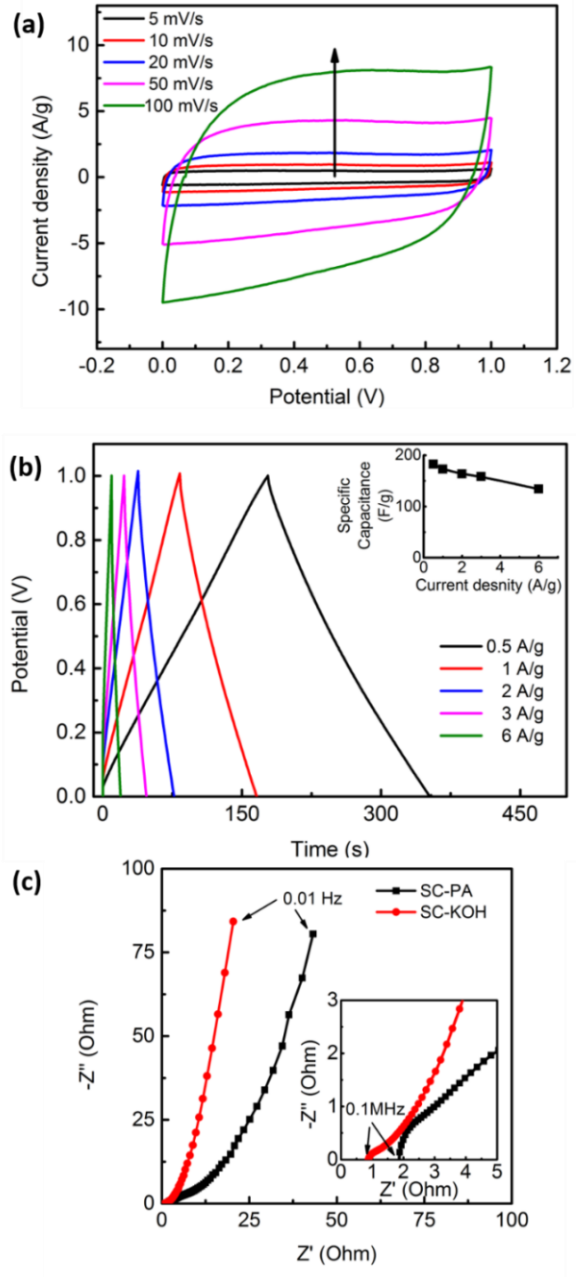

Figure S6. (a) Cyclic voltammetry (CV) profiles and (b) Galvanostatic charging–discharging (GCD) profile of SC-KOH (inset: specific capacitance verses current density). (c) Nyquist plot of EIS for SC-PA and SC-KOH. Descriptions can be found in the main text.

S7) Ragone plots of SC-PA and SC-KOH

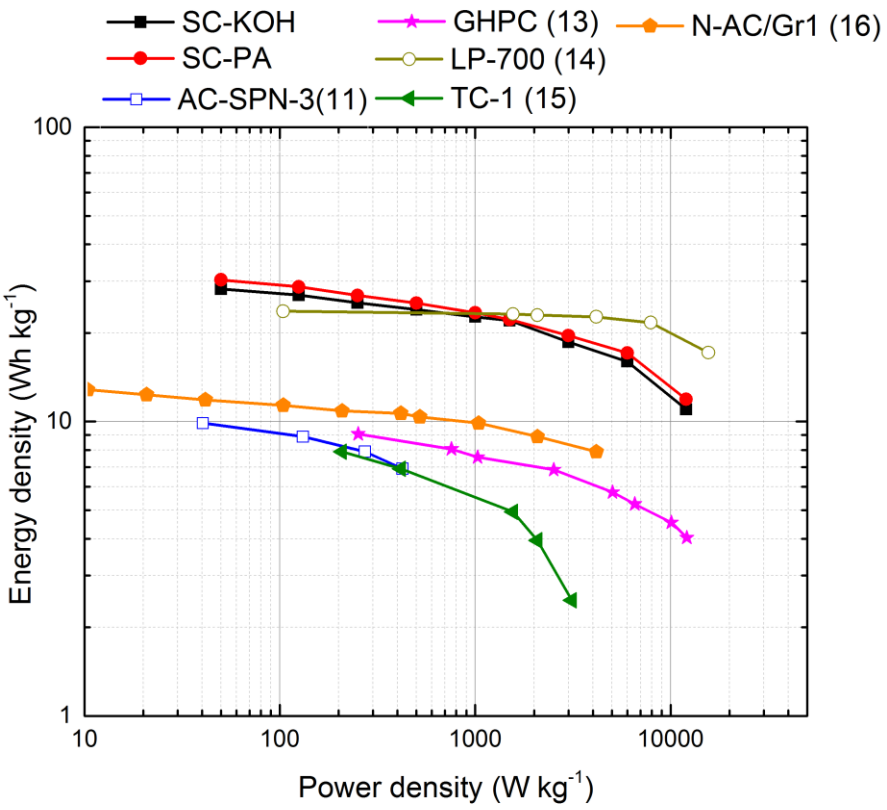

Figure S7. Performances of the SC-PA and SC-KOH devices were compared against previously published symmetric supercapacitors in references [11,13-16]. Here, the references used biomass-derived carbonaceous materials as electrodes whereas the electrolytes were in aqueous solution form.

S8) Low temperature performance of SC-KOH

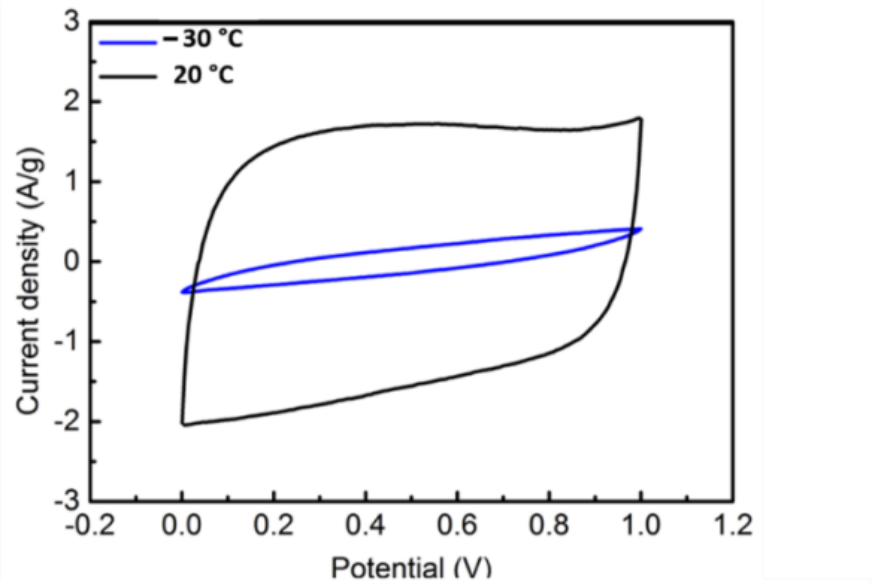

Figure S8. Cyclic voltammetry (CV) profiles of SC-KOH measured at 20 and –30 °C. The scanning rate was 20 mV s^{-1}.

S9) Flexibility and self-healing performance of SC-PA

To investigate the self-healing process for the supercapacitor, two broken parts of the SC-PA were aligned at the broken surface, followed by a mild heating and a pressure application. The setup used for SC-PA self-healing is shown in **Figure S9**. Broken SC-PA was stored in KOH solution at 30 °C. The glass slides and PTFE spacer were utilized to align the two broken pieces of the SC-PA.

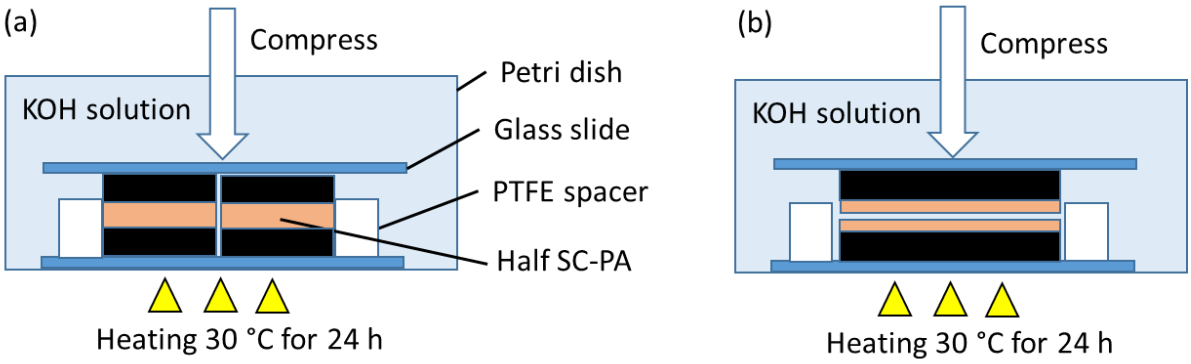

Figure S9. The experimental setup for the self-healing of SC-PA device. (a) SC-PA was cut into two pieces in the vertical direction (this describes the case for Figure 6c & d; perpendicular cut). (b) SC-PA was split into two pieces by slicing the polyampholyte hydrogel layer in the lateral direction (parallel cut).

References (for Supporting Information)

[1] B. Kumar, M. Asadi, D. Pisasale, S. Sinha-Ray, B. A. Rosen, R. Haasch, J. Abiade, A. L. Yarin, A. Salehi-Khojin, Renewable and metal-free carbon nanofibre catalysts for carbon dioxide reduction *Nat. Commun.* 4 (**2013)** 2819.

[2] J. Zhang, Z. Xia, L. Dai, Carbon-based electrocatalysts for advanced energy conversion and storage.*Sci. Adv.* 1 (**2015**) 1500564.

[3] D. R. Dreyer, S. Park, C. W. Bielawski, R. S. Ruoff, The chemistry of graphene oxide. Chem. Soc. Rev. 39 (**2010**) 228-240.

[4] X. Li, Y. Chen, A. Kumar, A. Mahmoud, J. A. Nychka, H.-J. Chung, Sponge-templated macroporous graphene network for piezoelectric ZnO nanogenerator. ACS Appl. Mater. & Interf. 7 (2015) 20753-20760.

[5] J. Jiang, L. Zhang, X. Wang, N. Holm, K. Rajagopalan, F. Chen, S. Ma, Highly ordered macroporous woody biochar with ultra-high carbon content as supercapacitor electrodes. Electrochim. Acta. 113 (2013) 481-489.

[6] G. Yu, L. Hu, N. Liu, H. Wang, M. Vosgueritchian, Y. Yang, Y. Cui, Z. Bao, Enhancing the supercapacitor performance of graphene/MnO2 nanostructured electrodes by conductive wrapping. *Nano Lett.* 11 (**2011**) 4438-4442.

[7] E. Raymundo-Piñero, F. Leroux, F. Béguin, A high-performance carbon for supercapacitors obtained by carbonization of a seaweed biopolymer. *Adv. Mater.* 18 (**2006)** 1877-1882.

[8] C. Casiraghi, A. Hartschuh, H. Qian, S. Piscanec, C. Georgi, A. Fasoli, K. Novoselov, D. Basko, A. Ferrari, Raman spectroscopy of graphene edges. *Nano Lett.* 9 (**2009)** 1433-1441.

[9] S. Stankovich, D. A. Dikin, R. D. Piner, K. A. Kohlhaas, A. Kleinhammes, Y. Jia, Y. Wu, S. T. Nguyen, R. S. Ruoff, Synthesis of graphene-based nanosheets via chemical reduction of exfoliated graphite oxide. *Carbon* 45 (**2007**) 1558-1565.

[10] M. Genovese, J. Jiang, K. Lian, N. Holm, High capacitive performance of exfoliated biochar nanosheets from biomass waste corn cob. J. Mater. Chem. A 3 (2015) 2903-2913.

[11] J. Xu, Q. Gao, Y. Zhang, Y. Tan, W. Tian, L. Zhu, L. Jiang, Preparing two-dimensional microporous carbon from Pistachio nutshell with high areal capacitance as supercapacitor materials. Sci. Rep. 4 (2014) 5545.

[12] J. T. Wang, C. Chen, E. Wang, Y. Kawazoe, A new carbon allotrope with six-fold helical chains in all-sp2 bonding networks. *Sci. Rep.* 4 (**2014**) 4339.

[13] Z. Zhu, H. Jiang, S. Guo, Q. Cheng, Y. Hu, C. Li, Dual tuning of biomass-derived hierarchical carbon nanostructures for supercapacitors: the role of balanced meso/microporosity and graphene. *Sci. Rep.* 5 (**2015**) 15936.

[14] K. L. Wang, Y. H. Cao, X. M. Wang, M. A. Castro, B. Luo, Z. R. Gu, J. Liu, J. D. Hoefelmeyer, Q. H. Fan, Rod-shape porous carbon derived from aniline modified lignin for symmetric supercapacitors *J. Power Sources* 307 (**2016**) 462-467.

[15] Y. Q. Zhao, M. Lu, P. Y. Tao, Y. J. Zhang, X. T. Gong, Z. Yang, G. Q. Zhang, H. L. Li*, Hierarchically porous and heteroatom doped carbon derived from tobacco rods for supercapacitors. J. Power Sources* 307 (**2016**) 391-400.

[16] Q. X. Xie, R. R. Bao, A. R. Zheng, Y. F. Zhang, S. H. Wu, C. Xie, P. Zhao, Sustainable low-cost green electrodes with high volumetric capacitance for aqueous symmetric supercapacitors with high energy density. *ACS Sustain. Chem. Eng.* 4 (**2016**) 1422-1430.

[17] Y. Zhu, S. Murali, M.D. Stoller, K.J. Ganesh, W. Cai, P.J. Ferreira, A. Pirkle, R.M. Wallace, K.A. Cychosz, M. Thommes, D. Su, E.A. Stach, R.A. Ruoff, Carbon-based supercapacitors produced by activation of graphene. *Science,* 332 (**2011)** 1537-1541.

[18] M. D. Stoller, R. S. Ruoff, Best practice methods for determining an electrode material's performance for ultracapacitors. *Energy Environ. Sci*. 3 **(2010)** 1294-1301.

[19] H. Huang, L. Xu, Y. Tang, S. Tang, Y. Du. Facile synthesis of nickel network supported three-dimensional graphene gel as a lightweight and binder-free electrode for high rate performance supercapacitor application. *Nanoscale* 6 **(2014)** 2426-2433.